# Evaluation and Compensation of the Effect of Dirt on Time-of-Flight 3D Imaging Systems

Zhibin Liu and Miguel Heredia Conde, *Member, IEEE*

***Abstract*—In the past few years, 3D imaging technology has received a lot of attention. Time-of-Flight (ToF) cameras based on the indirect ToF principle calculate depth information by measuring the phase shift between the emitted periodic signal and the reflected signal. When the illumination from the modulated light source reaches the same pixel through multiple paths, multipath interference will occur. Acquisitions at multiple modulation frequencies are then required to separate the interfering paths. Parametric spectral estimation methods, such as Prony's method and its robust variants, have shown success in resolving multiple paths from multi-frequency measurements. With the widespread usage of ToF cameras in various fields, the operating environment of the camera should be taken into account in order to obtain accurate 3D images. In this work, we aim to study the effect of dirt on 3D imaging systems quantitatively. To this end, ten sheets with different transmittances, between 50% and 100% are used. To the best of our knowledge, for the first time we provide standardized methods for evaluating the effect of dirt on protective covers in the depth estimation of "flash lidar". The accuracy of depth measurements obtained by multi-frequency multipath recovery in the absence of dust is up to 99%. However, when the light transmittance of the protective cover is less than 90%, the measurement result is already unreliable. The experiments have shown that the depth measurements obtained using the multi-frequency estimation method are more accurate in the presence of dust than the single-frequency estimation method.**

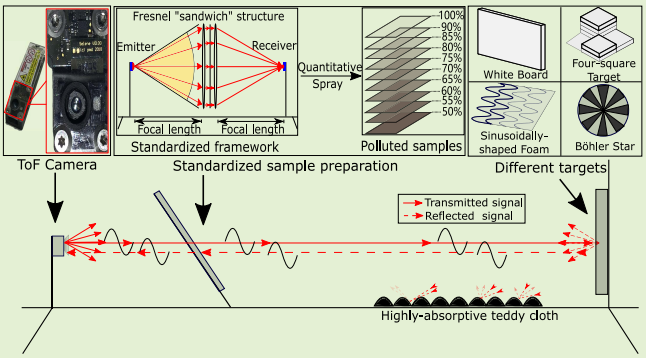


***Index Terms*— 3D imaging, ToF camera, effect of dirt, parametric spectral estimation methods, metrological evaluation.**

## I. Introduction

With the development of digital imaging technology, 3D imaging technology has attracted more and more attention. 3D imaging systems can obtain the complete geometric information of natural 3D scenes and use depth images to achieve accurate digitization of scenes, so as to achieve high-precision recognition, localization, reconstruction, scene understanding, and other key functions of machine vision. 3D vision techniques using triangulation include stereo vision and structured light technologies [1]. Their basic principle is to use the geometric parallax of a triangle to obtain information about the distance from the target to the camera. This method has high accuracy at close range, but the error becomes larger rapidly with increasing distance.

Manuscript received 22 April 2022; revised 27 June 2022; accepted 27 June 2022. Date of publication 15 July 2022; date of current version 15 August 2022. This work was supported by the Center for Sensor Systems of the University of Siegen and of pmdtechnologies AG. The associate editor coordinating the review of this article and approving it for publication was Dr. Brajesh Kumar Kaushik. *(Corresponding author: Miguel Heredia Conde.)*

The authors are with the Center for Sensor Systems, University of Siegen, 57076 Siegen, Germany (e-mail: zhibin.liu@student.uni-siegen.de; heredia@zess.uni-siegen.de).

Digital Object Identifier 10.1109/JSEN.2022.3189773

Different from stereo vision and structured light solutions, Time-of-Flight (ToF) camera modules generate an illumination control signal, which is used to drive a fast light source, so that it emits high-frequency amplitude-modulated near-infrared light. After the light is scattered by the scene objects, the receiver calculates the depth information by the phase shift or time difference between transmitted and received signals. The ToF technique is more stable in terms of error at different distances compared to triangulation. Most ToF sensors now use back-illuminated CMOS technology, significantly increasing the light-sensitive area and improving the photon collection rate. The response time can reach the nanosecond level, which can ensure high accuracy at long distances. Major ToF camera manufacturers include pmdtechnologies, MESA Imaging (Heptagon, ams), SoftKinetic-Optrima (Sony), Basler, meere-company, Analog Devices, Teledyne e2v, Lucid Vision Labs, and Microsoft [2]. ToF cameras are not only used for facial identification in mobile phones, but also in many other fields such as gesture-based human-computer interaction [3], [4], indoor surveillance [5], material sensing [6], [7], and automated driving [8].

According to the modulation scheme, ToF methods can be generally divided into pulse modulation and continuous-wave (CW) modulation. Pulse modulation requires a great overall

system bandwidth and the generation of high-intensity pulses at the transmitter side, which requires high physical device performance. Additionally, pulsed devices based on direct ToF principle, also require carrying out high-precision time measurements. The sensors based on discrete pulse modulation measure the round-trip time of the optical pulse to calculate depth, while the sensors based on the lock-in principle measure phase shift between the transmitted and received periodic signal [9]. Since the phase shift of the sinusoidally-modulated light is proportional to the distance of the object from the camera, the phase shift can be used to measure the distance.

### A. Motivation

With the widespread deployment of Advanced Driver Assistant Systems (ADAS) in vehicles, high-level ADAS have been able to perform many tasks in place of the driver. With the expectation of a more advanced level of ADAS as well as autonomous driving, the accuracy of sensor-based environment perception has become more demanding. Highly integrated ToF cameras are no longer limited to in-cabin applications (e.g., driver status monitoring) due to their small size, outstanding depth measurement performance, and low power consumption. ToF cameras are also taking their place in external applications (e.g., autonomous parking). The complexity and variability of the real environment introduce varying degrees of uncertainty into sensor measurements. The impact of weather and dust on the accuracy of LiDAR systems has been studied by major car manufacturers (e.g., Robert Bosch [32], BMW [29], Audi [30]). However, the effect of dirt on the performance of 3D cameras has been a gap so far. In order to obtain accurate 3D images, the operating environment of the ToF camera should be taken into account.

With the increasing maturity of 5G technology, low-latency information interaction offers the possibility of remote control. Unmanned vehicles in relatively closed scenarios will likely be tested first, and intelligent mines have become one of the scenarios with the strongest demand. The harsh environment is a double challenge for sensor hardware performance and autonomous driving perception algorithms. When the weather is sunny or rainy, the mining area is dusty or muddy, respectively. In addition, the road features are not obvious and the boundaries are not clear, unmanned mine trucks often cause emergency speed limits and stopping restrictions due to misidentification of dust. Therefore, the impact of dust in practical applications cannot be ignored. Studying the effect of dust on the performance of different types of sensors not only helps to explore the compensation of environmental interference problems in real industrial scenarios, thus accelerating the promotion of unmanned driving in industrial fields, but also serves as an experience accumulation for the popularization of autonomous driving in the future.

One of the most common problems the ToF technology faces is multipath interference (MPI) [10], [11], [13], [17], [18], [19], [20], [21], [22], [23], [24], [27]. Light is reflected multiple times in the target scene, and an object reflects not only the modulated light emitted by the camera, but also light from other indirect paths. A variety of scenarios can cause MPI. Four common scenarios leading to MPI are illustrated in Fig. 1. Fig. 1(a) shows that the existence of

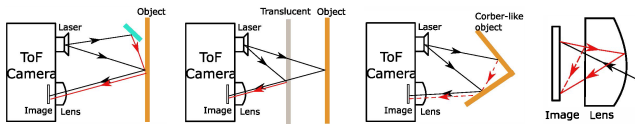


(a) Specular reflection. (b) Translucent reflection. (c) Corner-like objects reflection. (d) Inter-reflection inside the lens.

Fig. 1. The cause of MPI. The black line indicates the direct path and the red line indicates the interference path. (a) Reflective MPI is caused by highly reflective objects such as mirrors. (b) Translucent objects also produce MPI. (c) Corner-like objects lead to diffusive MPI. (d) Inter-reflection inside the lens also causes MPI.

highly reflective objects results in specular reflections in the scene. Considering the scenario in Fig. 1(b), the same ToF pixel receives both the direct return path from the target, plus an additional secondary path from the translucent sheet. In the case of corner-like objects (Fig. 1(c)), each point on the wall may receive reflected light from other points, which will be partially reflected back to the camera. The inter-reflection between the image sensor and the lens elements also contributes to MPI (Fig. 1(d)). The interference between reflected light from multiple sources can lead to errors in depth measurement. Retrieving multiple reflected paths with the help of multi-frequency approaches contributes to finding the true depth measurement. In practice, it is easier to implement a ToF system with sequential acquisition at different frequencies than a pulsed system that requires acquisition for different delays, since adjustable delays in the picosecond range with low jitter typically require external equipment that is both expensive and bulky.

### B. Related Work

Since the sinusoidally-modulated light is periodic with $2\pi$, for the CW-ToF camera, ambiguity errors arise due to phase wrapping when the measured distance exceeds half of the wavelength i.e., the maximum unambiguous range or unaliased distance, which is expressed as: $d_{\max} = \frac{c}{2f}$, where $c$ is the speed of light and $f$ is the modulated frequency. For single frequency modulation, the limited range of the ToF camera is dependent on the modulation frequency. Reducing the modulation frequency to avoid phase wrapping is a common approach, but this leads to a decrease in measurement accuracy [14]. The trade-off between measurement distance and measurement accuracy results in most ToF cameras having a measurement range within 10m. Multi-frequency technology enables the maximum unambiguous range to be extended while maintaining high accuracy. Different frequencies have different unambiguous ranges, and by comparing the depth measurements obtained at different frequencies, the correct unwrapped distance can be found that is common to all frequencies [15]. In [16], Jongenelen *et al.* demonstrated that dual frequency modulation can increase accuracy and extend the maximum unambiguous range. The maximum distance is determined by the greatest common divisor (GCD) of the multiple frequencies.

ToF cameras usually have errors when directly using the raw data for depth estimation due to systematic effects in the imaging pipeline, external environmental interference, etc.

Therefore, a series of calibrations of ToF cameras are needed to improve the measurement accuracy before application. A major systematic error of ToF cameras is the wiggling error. Due to the limitation of hardware complexity and cost, the transmitted signal is not a perfect sinusoidal signal. Besides the fundamental wave signal, it may also contain higher order harmonic components. Therefore, the imperfect sinusoidal signal in the demodulation process causes periodic errors between the measured phase difference and the ideal phase difference. In 2006, Lindner *et al.* [17] proposed a calibration method using B-spline fitting, which can achieve a precision of 10mm per pixel. The wiggling error compensation is performed by building an error lookup table in [18]. This method has high accuracy, but the accuracy of compensation depends on the size of the error lookup table. The compensation time depends on the implemented scheme. In the implementation in [18], the compensation time is far less than the real-time acquisition time, which makes it possible to acquire dynamic scenes.

In our experiments, since a dirty sensor cover produces multiple bounces that distort the ToF measurements, we also review existing research on multipath interference before specifically studying the effect of dirt on ToF 3D imaging systems. In [19], two methods of multipath interference separation were introduced. The first method can separate two paths making use of four measurements at different modulation frequencies. The other method uses attenuation ratios to determine the amplitude and phase of up to two paths. Bhandari *et al.* used orthogonal matching pursuit (OMP), which is an iterative algorithm, in [10] to implement a multi-frequency approach for decomposing multiple depths observed by a ToF camera in 2014. Apart from that, Bhandari *et al.* first explored pulse- and wave-based multi-frequency measurements and found that they are equivalent due to the linearity and superposition principles. Nevertheless, it should be noted that a pulse shape exhibits a sharp decay of signal power with frequency, thus compromising the SNR of the high frequencies in Fourier domain [12]. This can be avoided in a multi-frequency setup, like the one adopted in this paper. In [11], Bhandari *et al.* proposed a non-iterative method without any sparsity-inducing penalty term and solved the sparse linear operator identification problem via a parameter estimation method. In [20], a multi-frequency-based approach to analyze multipath models that solves the problem by processing the temporal variation of the original measurements for each pixel in the Fourier domain was reported, which used a similar principle as in [11]. The *matrix pencil method* was proposed in [21] and used to estimate the parameters of exponentially damped/undamped sine waves in noise. The method has been successfully applied in [22] and [23] for the depth super-resolution problem, which can be seen as the estimation of parameters for $K$ complex exponentials, where $K$ is the number of paths. In [22], Bhandari *et al.* provided a closed-form, non-iterative technique and proved that $2K+1$ frequency measurements are necessary for decomposing $K$ interfering paths. In [23], Bhandari *et al.* showed that the super-resolution problem in the context of ToF imaging can be re-formulated as a finite-rate-of-innovation sampling problem. The results provided in [23] showed that the calculation efficiency of

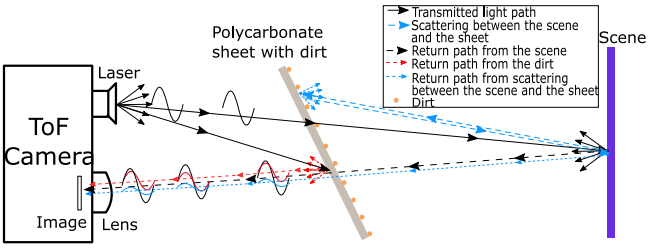


Fig. 2. The diagram of light path propagation when the sheet is polluted by dust. The scattering of light signals by dirt causes MPI in a 3D camera.

*matrix pencil method* is five times that of OMP. In [24], multi-frequency measurements are combined with a *compressive sensing* (CS) algorithm to reconstruct the sparse signal and thus retrieve the true depth. Instead of [24], which is a rather unfeasible approach, Heredia Conde *et al.* tuned and simplified the recovery process leveraging the knowledge of the structured sparsity of the recovered signal in [25] and [26], obtaining better accuracy and reducing the runtime compared to pure OMP recovery. However, this CS framework is considered not feasible because it involves not only large memory requirements but also heavy computational load [27]. In this work, we use parametric spectral estimation methods, more specifically the *matrix pencil method* [21], which is a robust variant of Prony's method (polynomial annihilation).

Some publications exist that study the influence of the weather and dirt on optical ranging sensors. In [29], Rasshofer *et al.* from BMW studied the effect of weather phenomena on lidar systems in 2011. By testing in real weather environments, artificial rainfall environments and electro-opticallaser radar target simulation, it was shown that their proposed electro-optical laser radar target simulator system (OSS) can have high accuracy in simulating laser radar performance in fog. Rivero *et al.*, from Audi's autonomous driving department, studied the effect of road dust on the performance of LiDAR in [30] in 2017. The samples were collected in the real world. The transmission and reflection in two different positions were investigated. In [31] the influence of weather effects, in particular rain droplets, on distance and depth measurements obtained with a ToF camera-based sensor are examined based on optical simulation models in 2017. Trierweiler *et al.* from Robert Bosch obtained an almost-homogeneous distribution of dust on polycarbonate sheets resulting in a maximal range decrement of 25% in [32]. In 2020, a ToF LiDAR operating within a foggy environment was presented in [33], where performance is qualitatively and quantitatively investigated. A prediction model based on machine learning to the minimum fog visibility is introduced, which is trained on collected data.

### C. Contributions of This Paper

Unlike [30] and [32] focusing on performance analysis of non-quantitative dirt on sensor, in this paper, we aim at providing a standardized framework for the characterization of the effect of dirt on 3D imaging systems. The main contributions of this papers work are summarized as follows:

*1) Reframing the Dirt Problem:* The effect of dirt on the surface of the sheet on light propagation is shown in Fig. 2.

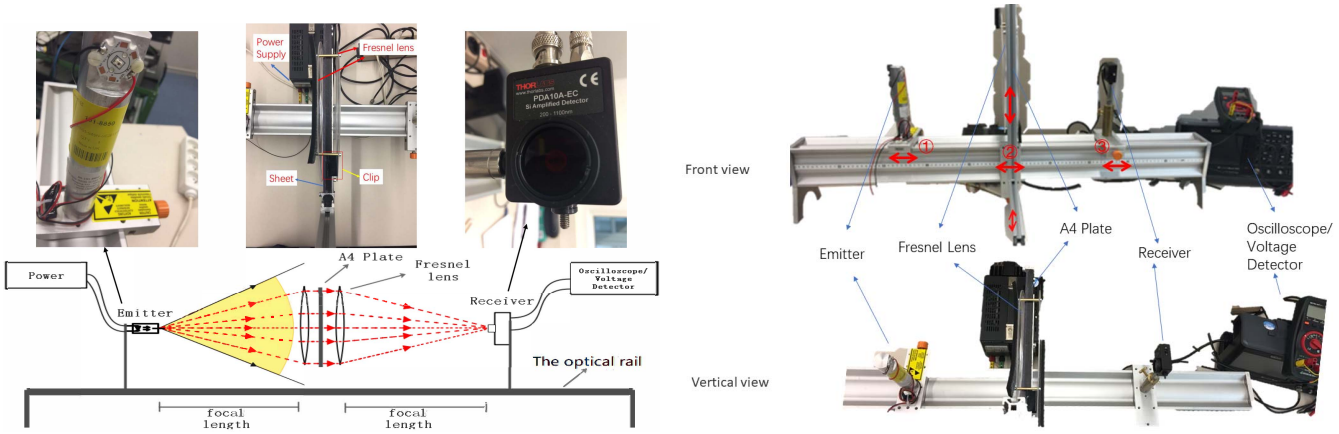


(a) Sketch of optical setup

(b) Front and vertical view of real optical setup

Fig. 3. The optical setup for obtaining quantitative transmittance of an A4-sized sheet. The emitter, the Fresnel lenses with "sandwich" structure, and the receiver connected to a digital multimeter measuring voltage are fixed in the optical rail from left to right.

Dirt attached to the surface of the polycarbonate sheet not only attenuates the transmitted signal but also causes the signal to be scattered on the sheet surface due to dirt particles obstructing the transmitted signal, resulting in the measurement at the observation point being the sum of multiple optical paths (returns from both the scene and the sheet). The polluted sheet acts just as the translucent sheet in Fig 1(b). Hence, the effect of dust on 3D camera performance can be regarded as a MPI problem. Consequently, the dirt problem can be addressed by parametric spectral estimation methods [11], [22], [23], [27]. The ToF system operating in Amplitude Modulated Continuous Wave (AMCW) mode does not require bulky and expensive external equipment compared to pulse-based multi-frequency measurements. Real-time needs to be taken into account in practical applications. The calculation time depends on the number of reflected paths $K$. For the case of retrieving the same number of reflected paths, the multi-frequency method we use is the fastest. With the help of the *matrix pencil method* the computational efficiency is higher than OMP and LASSO. Comparisons of the computation times of the different algorithms are presented in [11], [23], and [28]. When considering the recovered phase shift for the dominant path, the multi-frequency approach we use can check the degradation of the camera's performance in different different operation areas in real-time [35].

*2) Quantitative Performance Analysis:* Exploiting the accurate knowledge of the light transmittance of each sample, we can quantitatively analyze the performance of the ToF camera at different light transmittance and at different distances. Thus, we define different regions of operation, as a function of dirt and distance to target, based on the observed decay of the camera's performance.

*3) Metrological Evaluation and Compensation:* We investigate the performance of the camera in the different operation areas when facing different experimental targets (white board, panel containing sinusoidally-shaped foam and four-square target, and Böhler star), aimed to evaluate relevant metrological parameters, and demonstrate that the adopted multi-frequency approach performs better than single-frequency methods under the effect of dust.

The remainder of this paper is organized as follows: section II presents the optical setup for acquiring standardized samples, the experimental setup for data acquisitions, and a brief principle of operation of a ToF camera. Standardized sample preparation and acquisition of experimental data are described in section III. The results are discussed in section IV, and the performance of the ToF camera is also analyzed. Finally, section V concludes the paper and outlines future work.

## II. Core Models and Techniques

In this section, we describe the optical setup for preparing standardized samples (polycarbonate sheets with customized transmittance), the experimental setup model for acquiring experimental data and the corresponding tools, and the operating principle of the ToF camera.

### A. Optical Setup

In order to accurately characterize the effect of different dirt concentrations on the transmittance, a near-infrared light source is used as emitter (model ILH-IS01-94SN-SC201-WIR200), a Thorlabs PDA10A-EC photodiode as receiver, and two Fresnel lenses to ensure orthogonal light incidence, as illustrated in Fig.3.

An aluminium holder with the NIR emitter was fixed at the focal point of the first Fresnel lens, and the first Fresnel lens was used to obtain collimated light over a large aperture (preferably the whole A4 sheet) and the second Fresnel lens to focus the collimated light passing through the sample to a point where the holder with receiver was placed. The Fresnel lens model is ORAFOL's SC210. The SC210 has a focal length of 225.5mm and an aperture of 257.6mm and is suitable for the A4-sized polycarbonate sheets we use.

To realize the aforementioned setup, a Fresnel "sandwich" structure was designed and constructed, as shown in Fig.3(a) The structure allows for an A4-sized polycarbonate sheet to be inserted between the two Fresnel lenses. Note that the center of the A4-sized sheet is aligned with the center of the Fresnel lens. The holder's height was adjusted so that the center of the transmitter, receiver, sheet, and Fresnel lenses were in one

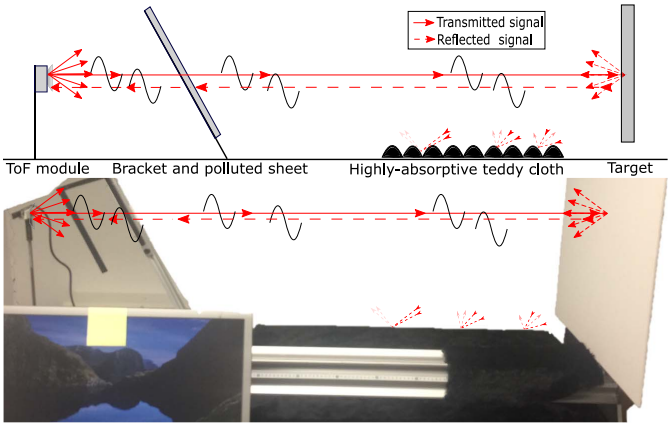


Fig. 4. The sketch of the setup for data acquisition and the real setup on the optical table in a dark room. From left to right are the ToF camera, the tilted shelf bracket, and the target object.

horizontal straight line. The two lenses were connected by four 3cm long screws.

## B. Experimental Setup

All experimental procedures were carried out in a dark room. The outline and real diagram of the setup are shown in Fig.4. The rail, the optical table, and the background wall are wrapped with highly-absorptive teddy cloth to reduce the interference due to uncontrolled multipath effects. The camera is a "Selene" module from the company pmdtechnologies AG, which was used in the live demonstration [35]. Compared with other reflected photons from the target, the photons, which are reflected directly on the sheet's surface, have the shortest path. Depending on the incidence and exit directions, the reflected light can be of higher or lower intensity. This is due to the (close to) specular behavior of the sheet surface. Specular reflection means that photons get scattered back primarily along a direction that forms the same angle with the surface as the incidence direction. This can "blind" an imaging sensor if such a sheet is placed perpendicularly to the line of sight of the camera. The tilted bracket avoids that the specular reflection from the sheet blinds the camera. The initial distance between the center of the ToF camera and the target is 50cm. The position and height of the camera and the bracket are fixed, so that the camera is aligned with the center of the bracket. Between the camera and the target one sheet is placed in the bracket with the desired transmittance. The distance between the center of the camera and the center of the sheet is 20cm.

To evaluate the different performance indicators of the camera, we chose four different targets.

*1) White Board:* The white board in Fig.5(a) is flat, textureless, and completely opaque. The white board is a standard test target for measuring depth accuracy at different distances with different light transmittance.

*2) Four-Square Target:* The four-square target in Fig.5(b) consists of a ground plane and three 5cm × 5cm cubic squares. Each square is formed by superimposing a different number of layers of the same height (3.5mm). The upper-left square has four layers accounting for a total height of 14mm. The upper-right square has one layer of 3.5mm height. The lower-left is the ground plane. The lower-right square has two

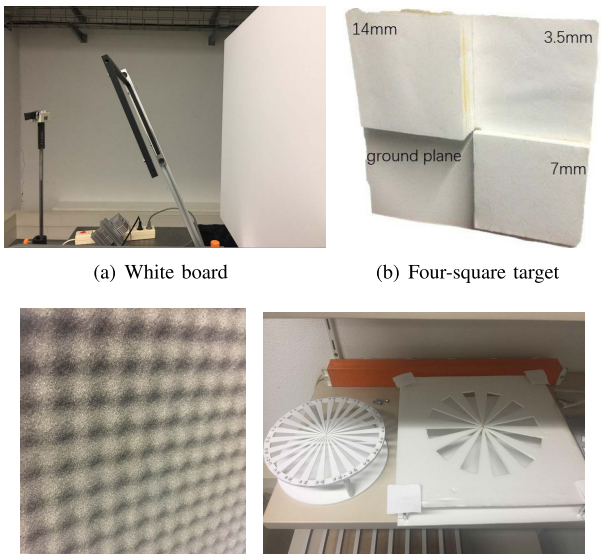


(a) White board (b) Four-square target

(c) Sinusoidally-shaped foam (d) Böhler stars

Fig. 5. The four different targets considered in our experiments.

layers accounting for a total height of 7mm. The four-square target allows for testing the capability of resolving small depth differences.

*3) Sinusoidally-Shaped Foam:* The sinusoidally-shaped foam in Fig.5(c) has a surface that resembles a 2D sinusoid with an amplitude of 2.5cm and a wavelength of 4.5cm. The sinusoidally-shaped foam allows for testing the overall capability of reconstructing complex 3D shapes.

*4) Böhler Stars:* The Böhler stars in Fig.5(d) are both of 20cm diameter. The left star features 48 fields, and the right one 24. The Böhler star is a crucial target for measuring the real lateral resolution of the camera.

## C. Operating Principle of the ToF Camera

In this work, we mainly study ToF systems working in AMCW mode. We present the results for mono-frequency estimation of a single path applying the four phases algorithm [36], [37] and multi-frequency estimation of several paths using the *matrix pencil method* [21] as parametric multipath estimation algorithm. In the mono-frequency case, one emits $s(t)$ and receives $r(t)$:

$$s(t) = 1 + \lambda \cos(\omega t) \tag{1}$$
$$r(t) = A(1 + \lambda \cos(\omega t - \phi)) \tag{2}$$

where $\lambda$ is the modulation depth and $\omega$ is the angular frequency of modulation of the light source. A is the amplitude of the reflection. $\phi$ is the delay between the transmitted signal and the reflected signal. The distance between camera and reflector is then

$$d = c\phi/2\omega \tag{3}$$

where $c$ is the speed of light. A continuous wave ToF sensor measures the correlation function between the two signals.

$$\begin{aligned} m_\omega(\tau_q) &= (s(t) \otimes r(t))(\tau_q) \\ &= A\left(1 + \frac{\lambda^2}{2}\cos(\omega\tau_q + \phi)\right) \end{aligned} \tag{4}$$

where $\otimes$ denotes cross-correlation. By using the "four-phases algorithm", we can calculate the amplitude A, the phase shift $\phi$, and the offset B. Using four samples at $\tau_q = \pi q/4\omega$ with q = 0, …3:

$$A = \sqrt{(m_\omega(\tau_3) - m_\omega(\tau_1))^2 + (m_\omega(\tau_0) - m_\omega(\tau_2))^2}/\lambda \tag{5}$$

$$\tan\phi = \left(\frac{m_\omega(\tau_3) - m_\omega(\tau_1)}{m_\omega(\tau_0) - m_\omega(\tau_2)}\right) \tag{6}$$

Therefore, the obtained values of amplitude and phase can be jointly represented by the following complex number:

$$Z_\omega = Ae^{j\phi(\omega)} \tag{7}$$

In the multiple-path case, by virtue of the superposition principle, (7) now becomes a sum of complex exponentials.

$$Z(\omega) = \sum_{k=1}^{K} A_k e^{j\phi_k(\omega)}. \tag{8}$$

where the phase delay corresponding to each reflection path $K$ is $\phi_k(\omega) = 2d_k\omega/c$. $\{d_k\}_{k=1}^K$ and $\{A_k\}_{k=1}^K$ are the depths and amplitudes at which the corresponding reflection occurs, respectively. A general description of the ToF image formation model is provided in [22], [23], and [38].

## III. Experiments

In this section, we focus on the preparation of standardized samples using the optical setup and detail our experiments to evaluate the camera's performance using the obtained standardized samples.

### A. Standardized Sample Preparation

In this research, we aim to evaluate the effect of dirt on ToF cameras when operating outdoors, e.g., in automotive applications or mobile robotics. We present methods developed to obtain samples of dirty polycarbonate sheets of custom transmittance. Polycarbonate as the substrate material is selected because it is commonly used as a protective cover for sensors. Trierweiler *et al.* used the same material as the substrate for the five samples obtained in [32]. In our experiments, we use ten transparent polycarbonate sheets of size A4. The transmittance of each sheet can be customized to enable a quantitative evaluation of the effect of dust on the 3D imaging system.

Following the SAE J726 Rev. JUN93 standard [34], we chose *Arizona dust SAE J726 fine* as source of pollution. We used a spray gun in order to spray a mixture of dust and water homogeneously onto the surface of the sample. The dust is homogeneously mixed with water, and the deposit of the spray gun is filled with the resulting mix. One of the sheets is completely clean, and its transmittance is considered 100%. The transmittance of the remaining nine sheets is decreased by 5% for each new sample, from 90% to 50%. The specific operation and measurement pipeline for obtaining a sheet with target transmittance $T_d \in [50\%, 55\%, \ldots 90\%]$ are as follows:

1) Prepare a mixture with appropriate solution concentrations e. g. 10%, 17.5%, 20%.
2) Insert the blank sheet according to the above explanation in Section II-A. Record the voltage $V_0$ as a reference by means of a digital multimeter.
3) Before spraying, the mixture must be mixed homogeneously, and the spray gun must be warmed up. Adjust the nozzle of the spray gun until fine water particles are sprayed.
4) Spray the whole sheet thoroughly and uniformly.
5) Wait until it dries.
6) Insert the sprayed sheet. Record the voltage $V_i$. The current transmittance $T$ is $T = \frac{V_i}{V_o} \times 100\%$.
   If $T = T_d$, the polluted sheet has the desired transmittance. End the process and store the sample.
   If $T > T_d$, repeat the cycle of spraying from 3) to 6) until the $T = T_d$.
   If $T < T_d$, clean the dirt, repeat the cycle from 2) to 6) until $T = T_d$.

TABLE I
Transmission Data of the Polluted Samples

| Sheet No. | Original $V_0$ (V) / Final Voltage $V_i$ (V) | Transmittance $T$ |
|---|---|---|
| 0(Ref.) | 0.959 / —— | 100% |
| 1 | 0.954 / 0.858 | 89.9% |
| 2 | 0.974 / 0.832 | 85.4% |
| 3 | 0.962 / 0.774 | 80.5% |
| 4 | 0.951 / 0.711 | 74.8% |
| 5 | 0.968 / 0.667 | 69.6% |
| 6 | 0.961 / 0.626 | 65.1% |
| 7 | 0.950 / 0.575 | 60.5% |
| 8 | 0.957 / 0.526 | 55.0% |
| 9 | 0.947 / 0.473 | 49.9% |

We use a METRAHIT 27I multimeter for performing the voltage measurements. For testing purposes, three different concentrations of the solution (10%, 17.5%, and 20% volume of dust in water.) were used to study the effect of each deposited dust layer on the transmittance of the sample being generated. When the solution concentration is 20%, each spray results in a decrease in light transmission of more than 1%. Meanwhile, when the solution concentration is 10% or 17.5%, each spray causes a decrease in light transmittance of less than 0.1% or 0.3% - 0.4%, respectively. The change in light transmittance caused by the one-time spraying with a 10% concentration solution was too close to the resolution limit imposed by the multimeter. Hence, a solution concentration of 17.5% was chosen to be used in this study in order to allow for fine adjustment of the transmittance.

After each cycle of spraying and drying, the transmittance of the sheet is recalculated. After several cycles of spraying and drying, the sheets containing the desired light transmittance are generated, which are between 50% and 90%. The polluted sheets are shown in Fig.6. The light transmission measurements obtained for each sample are given in Table.I. The original voltage $V_0$ is between 0.95 V and 0.97 V except sheet No.2 with 0.974 V. The error of transmittance $\Delta T = \frac{|T_d - T|}{T_d} \times 100\%$ is under 0.5%.

### B. Experimental Data Acquisition

In the experimental data acquisition, we mainly compare the differences between single-frequency estimation and

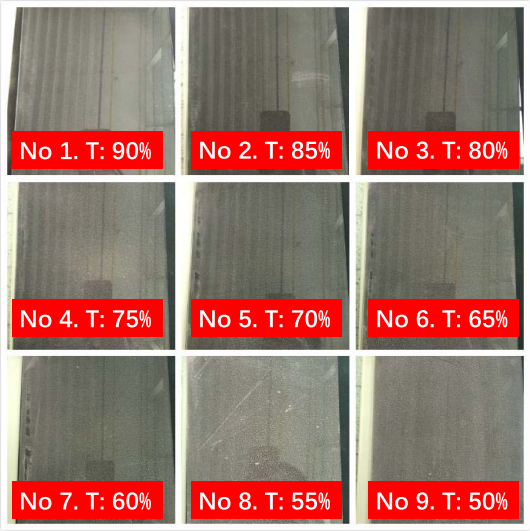


Fig. 6. The polluted samples with their transmittance.

multi-frequency estimation. In the single-frequency estimation we consider the cases at the minimum and maximum frequencies. Since the use of multiple frequencies enables the differentiation of multiple paths, we consider three cases for solving the inverse problem, i.e., with a maximum of three reflected paths. $K$ indicates the number of reflected paths. Path $P_i$, $i \in [1, K]$ denotes the specific reflected path. One considers a single dominant return path, $K = 1$ and considers the contribution along the secondary path as unmodeled disturbances. The second one considers the existence of a secondary path, $K = 2$, and tries to disentangle them (path $P_1$ and path $P_2$). The third one considers two secondary paths $K$=3, and tries to separate them (path $P_1$, path $P_2$ and path $P_3$). We resolved multiple paths directly from multi-frequency data acquired at $n_{\text{freq}} = 7$ equally-spaced frequencies from 0 to 120MHz (20MHz step size). The data acquisition process is shown below:

1) Place a target at a distance of 50cm from the ToF camera.
2) Hang the sheets with different transmittance in sequence [100%, 90%, 85%, …50%] and record the multi-frequency ToF raw data for each of them.
3) Move the target horizontally to the right 10cm each time, repeat step 2) until the distance between the target and the camera is 140cm.
4) Save data $D_i(m, n)$, where $i$ represents the sequence of the target, $i \in [1, 4]$. $m$ and $n$ represent the sequence of transmittance and the sequence of distance, respectively. $m, n \in [0, 9]$.
5) Replace the target with a new one and repeat steps 1) to 4).

Note that each data item, $D_i(m, n) \in \mathbb{C}^{n_{\text{rows}} \times n_{\text{cols}} \times n_{\text{freq}}}$, is a 3D tensor containing complex meaurements at each frequency for each of the $n_{\text{rows}} \times n_{\text{cols}}$ pixels of the ToF array. In our case, the "Selene" module features a high-resolution ToF pixel array of 172 × 224 px, so here $D_i(m, n) \in \mathbb{C}^{172 \times 224 \times 7}$.

We tested four different targets in Fig.5 following the above steps to acquire the corresponding data.

## IV. Results

### A. White Board

In Fig. 7, we show the experimental results at a distance of 50cm without the effect of dirt not only for the single-frequency estimation but also for each path for the multi-frequency estimation. From Fig.7 we can conclude that the higher the reflected amplitudes, the higher the depth accuracy. Low amplitude often appears at the edge of the image because the emitted light power decays radially, resulting in an overestimation of depth. In the mono-frequency case, i.e., $f_{\min} = 20$MHz and $f_{\max} = 120$MHz, the difference in depth between the central area and the corners of both depth images is greater than 1cm. In contrast, in the case of multi-frequency multipath recovery, whether in single path $K = 1$, multipath $K = 2$ path $P_1$, or multipath $K = 3$ path $P_1$, the difference in depth between the central area and the corners is less than 0.7cm.

Fig.8 demonstrates the measurement error for each path versus transmittance and distance in the multi-frequency multipath recovery. In the case of $K = 1$ (Fig.8(a)) and multipath $K = 2$ path $P_1$ (Fig.8(b)), without the effect of dirt the accuracy of the depth measurements in the interval of 50cm to 140cm is 99%- 99.7%. The accuracy of the ToF camera hardly varies with increasing distance.

Comparing Fig.8(a) and Fig.8(b), it is observed that the measurement error of the ToF camera has approximately identical characteristics with the variation of transmittance and distance. Although in the case of multipath $K = 2$, path $P_1$ cannot obtain accurate measurements in the presence of dust, retrieving the path $P_2$ can obtain good results under the presence of dust (the dark blue area in Fig.8(c)) with an accuracy of up to 90%. Furthermore, compared to a single path that is completely blocked by dirt, the two paths allow for estimating the depth with a greater degree of accuracy in the presence of dust.

In our experiments we used six non-zero frequencies, which theoretically enable the exact separation of up to three paths. In practice, it was observed that adding two secondary reflectors, that is, two dirty polycarbonate covers at two different locations is not realistic. As it can be observed in Fig. 8(a), a single dirty cover already produces a major degradation in the estimation of the depth values for fairly high transmittances. This is as opposed to clean translucent sheets, used in [10]. When using clean translucent sheets one may hope to recover up to two secondary paths, apart from the target, i.e., three paths [10], [35]. Nevertheless, we have studied if aiming to retrieve three paths when a single dirty cover is present yields any improvements, e.g., by accounting for unmodelled secondary reflections in the experimental setup. Due to the presence of noise in the measurements and the negligible amplitude of the third reflection, the accuracy of depth estimates in the absence of dust is only 80% at best. By comparing Fig.8(d), Fig.8(e) and Fig.8(f), we found that in the case of multipath $K = 3$, none of the paths can accurately describe the true depth with the influence of dirt.

At the light of the above experimental results, we think that the practical significance of studying the case of two paths induced by the presence of dust on the sensor cover is

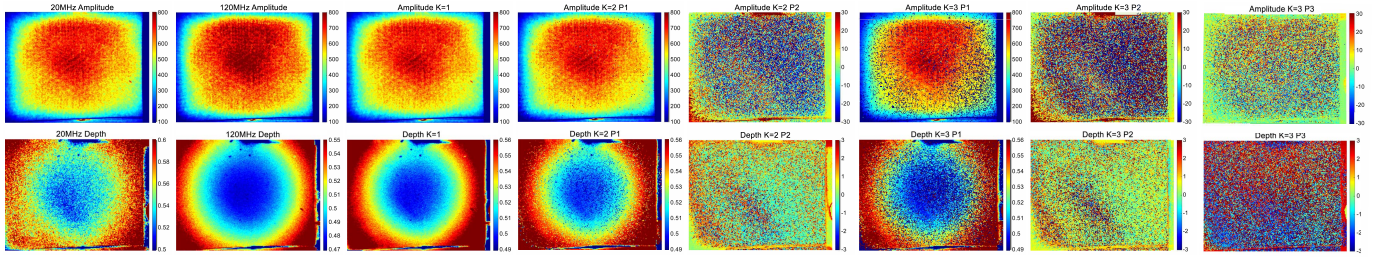


(a) 20 MHz (b) 120 MHz (c) $K = 1$ (d) $K = 2$, $P_1$ (e) $K = 2$, $P_2$ (f) $K = 3$, $P_1$ (g) $K = 3$, $P_2$ (h) $K = 3$, $P_3$

Fig. 7. Results obtained when observing a white panel at a distance of 50 cm from the camera, through a sample with 100% light transmittance, using (a) the "four phases algorithm" at the minimum frequency $f_{min}$ = 20 MHz and (b) maximum frequency $f_{max}$ = 120 MHz; (c)-(e) multi-frequency estimation of several paths for (c) $K$ = 1, (d)-(e) $K$ = 2 ($P_1$, $P_2$), and (f)-(h) $K$= 3 ($P_1$, $P_2$, $P_3$).

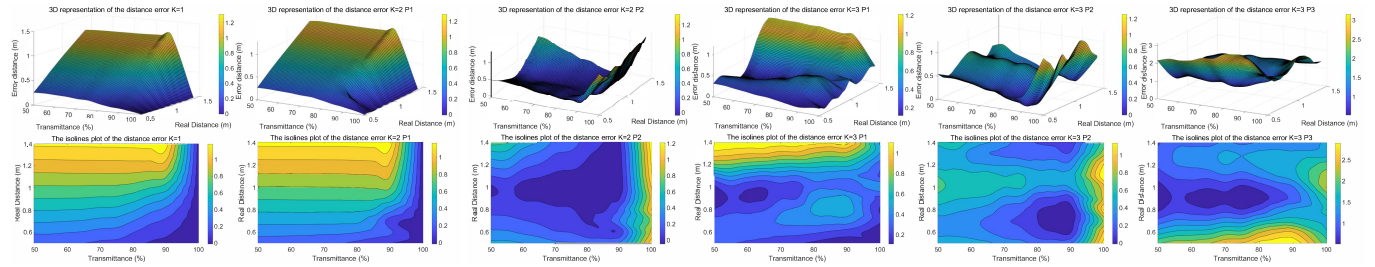


(a) $K = 1$ (b) $K = 2$, $P_1$ (c) $K = 2$, $P_2$ (d) $K = 3$, $P_1$ (e) $K = 3$, $P_2$ (f) $K = 3$, $P_3$

Fig. 8. 3D representation of the distance error versus transmittance and distance and the isoline plot of distance error. Multi-frequency estimation of several paths for (a) $K$ = 1, (b)-(c) $K$ = 2 ($P_1$, $P_2$), and (d)-(f) $K$ = 3 ($P_1$, $P_2$, $P_3$).

greater than studying more paths. Therefore, in the subsequent discussion, we focus mainly on the case of $K = 2$. When the sheet's transmittance drops to 95%, the accuracy of the depth measurements is reduced to less than 80% at a distance of 80cm. However, at a distance of 50cm a depth accuracy drop down to 80% is only observed for a sheet transmittance as low as 87%.

Depending on the limited operating conditions of the camera in terms of varying light transmittance and distance, we divided the camera operation into three stages in Fig.9. Fig. 9(a) and Fig. 9(b) show the case of multi-frequency estimation with $K = 2$ for path $P_1$ and $P_2$, respectively. In Fig.9(a), we defined that the area to the left of the red line is the *invalid* work area of the camera (the accuracy of the depth measurements is lower than 70%). The result of the depth measurements within this area is approximately equal to the distance between the camera and the sheet, i.e., about 20cm, because the dirt on the sheet has blocked most of the light, either in its way to the target or in its return path after being scattered by the target. The area between the red and white lines is the *unreliable* work area of the camera (the accuracy of the depth measurements is between 70% and 90%). The accuracy of camera measurements in this area is significantly affected by dirt. The area to the right of the white line is the *reliable* work area of the camera (the accuracy of the depth measurements is higher than 90%). The depth measurements obtained by the camera in this area in the absence of dirt or at a short distance (within 50cm) with an almost dirt-free environment (the transmittance is higher than 90%) are reliable. In Fig.9(b), since path $P_1$ in the *reliable* work area of the camera can retrieve the true depth, only

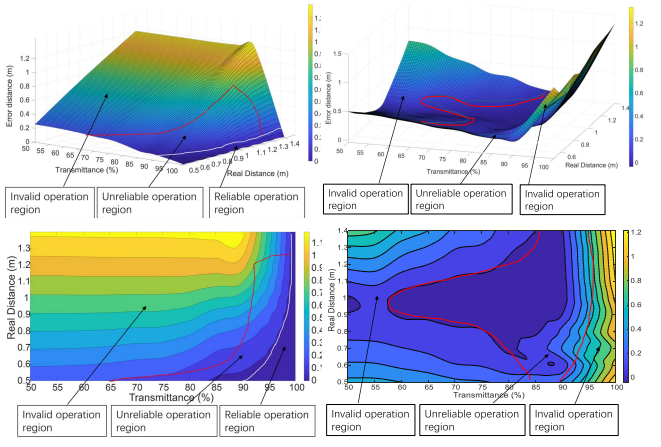


(a) $K$ = 2, $P_1$ (b) $K$ = 2, $P_2$

Fig. 9. 3D representation of the distance error versus transmittance and distance and the isoline plot of distance error. The images are divided into three parts by the red and white lines. These three parts are named as the *invalid*, *unreliable*, and *reliable* operation regions. (a) in the case of multi-frequency multipath recovery with $K$ = 2, path $P_1$. (b) in the case of multi-frequency multipath recovery with $K$ = 2, path $P_2$.

invalid depth measurements can be retrieved in path $P_2$, so the *reliable* work area becomes the *invalid* work area in the case of path $P_2$. In the presence of dust, path $P_1$ cannot retrieve the true depth properly due to the severe influence of dust. However, path $P_2$ allows to retrieve depth information with a maximum of 90% accuracy in the presence of dust, which means that the *unreliable* work area is extended by path $P_2$.

From the above comparison we can conclude that the single-frequency method and the single-path case cannot

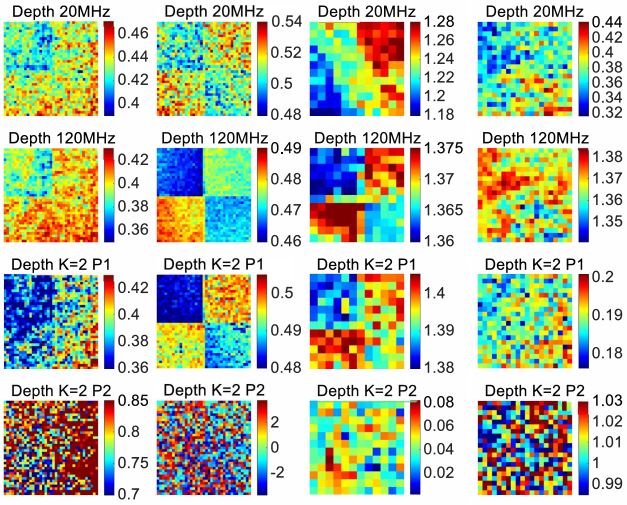


(a) 90%, 50 cm (b) 100%, 50 cm (c) 100%, 140 cm (d) 80%, 100 cm

Fig. 10. Four-square target depth plots. Along the row direction the effect of different distances and transmittances on the camera performance can be compared with the same measurement method. Along the column direction the effect of different measurement methods on the measurement accuracy can be compared under the same distance and transmittance.

accurately perform depth estimates even under the influence of fine dust (90% transmittance). The multi-frequency approach can break the limitation of the single-frequency (and single-path case) to cope with dust pollution to some extent due to the ability to retrieve multiple reflected paths. Also we can reach the same conclusion as in [27]. Even in the absence of dust, the multi-frequency method outperforms the single-frequency method.

### B. Four-Square Target

The four squares can be understood as four white boards. Therefore, the phenomena we observed in the whiteboard experiment will theoretically appear here. The effect of dirt on depth resolution is very relevant. With the increase of distance, the boundaries of the four squares have become increasingly difficult to distinguish. Compare the first row and second row in Fig.10: increasing the modulation frequency enhances the precision of the depth measurements. In the case of multi-frequency multilpath recovery with $K = 2$ for path $P_1$, the measured four squares are obviously more accurate than those measured by a single frequency. This illustrates that the multi-frequency method is preferable to the single-frequency approach even for a single return path. Nevertheless, when dirt exists, comparing Fig.10(a) and Fig.10(b), for instance, shows that the 10% reduction in transmittance directly results in the four squares being indistinguishable. As can be observed in Fig.10(d), at a distance of 100cm under 80% light transmittance, neither the single-frequency method nor the multi-frequency method can clearly distinguish the boundaries of the four squares. However, the accuracy of the estimated depth from the path $P_2$ of the multi-frequency method with $K = 2$ is higher than the accuracy of the single-frequency method.

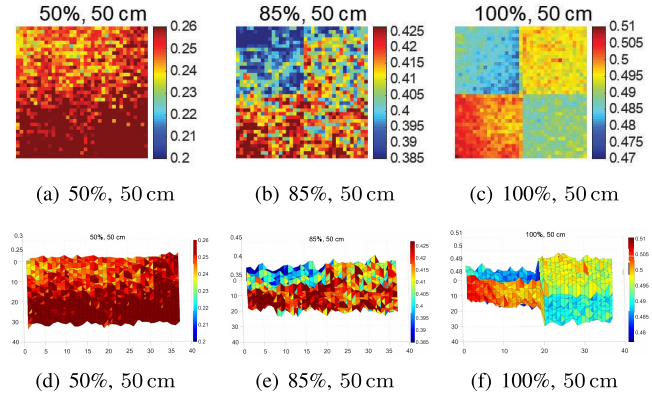


(a) 50%, 50 cm (b) 85%, 50 cm (c) 100%, 50 cm

(d) 50%, 50 cm (e) 85%, 50 cm (f) 100%, 50 cm

Fig. 11. Four-square target depth plots and corresponding surface plots in the case of multi-frequency estimation with $K = 1$ at 50 cm distance. The first row shows the depth plots and the second row shows the surface plots. For (a) and (d) the camera works in the invalid operation region (with 50% transmittance). For (b) and (e) the camera works in the unreliable operation region (with 85% transmittance). For (c) and (f) the camera works in the reliable operation region (with 100% transmittance).

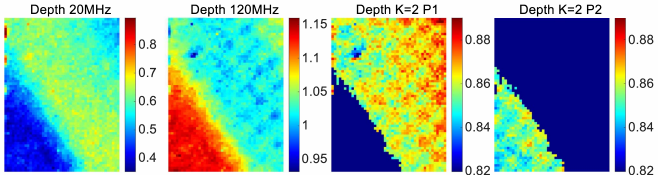


(a) 20 MHz (b) 120 MHz (c) $K = 2$, $P_1$ (d) $K = 2$, $P_2$

Fig. 12. Results obtained when observing a sinusoidally-shaped foam at a distance of 90 cm from the camera, through a sample with 100% light transmittance, using (a) the "four phases algorithm" at the minimum frequency $f_{min}$ = 20 MHz and (b) maximum frequency $f_{max}$ = 120MHz; multi-frequency estimation of two-paths for (c) path $P_1$ and (d) path $P_2$.

In this experiment, we are mainly interested in the height difference between squares. When the camera works in the invalid region, the depth estimation in Fig.11(a) is estimated to be approximately equal to the distance between the camera and the sheet due to a large amount of dirt adhering to the sheet. Therefore, the height difference between the four squares is small in Fig.11(d). When the camera works in the unreliable operation region, the depth estimation in Fig.11(b) can be obtained, due to a small amount of dirt, but it is unreliable. The height difference between the four-layers square and the ground plane can be clearly observed in Fig.11(e), but the values of this height difference is unreliable. When the camera works in the reliable operation region, the accuracy of the depth estimation in Fig.11(c) is higher than 90%. The height difference between the four squares can be calculated more accurately, and the four squares can be distinguished clearly in Fig.11(f). The results demonstrate that the ToF camera has the capability of resolving small depth differences in the absence of dust. However, as the effect of dust intensifies, this capability decreases dramatically, eventually leading to the impossibility of resolving small depth differences.

### C. Sinusoidally-Shaped Foam

Due to the unique surface structure of the sinusoidally-shaped foam, the single-path assumption yields invalid results

TABLE II
EMPIRICAL VALUES OF AXIAL RESOLUTION AND ANGULAR RESOLUTION IN DIFFERENT CASES

| Distance (cm) | Transmittance | Fields of Böhler Star | Axial resolution (cm) | | | Angular resolution (degrees) | | |
|---|---|---|---|---|---|---|---|---|
| | | | 20 MHz | 120 MHz | $K = 1$ | 20 MHz | 120 MHz | $K = 1$ |
| 50 | 100% | 24 | 0.3236 ± 0.0588 | 0.3236 ± 0.0588 | 0.2942 ± 0.0588 | 0.0065 ± 0.0012 | 0.0065 ± 0.0012 | 0.0059 ± 0.0012 |
| | | 48 | 0.3740 ± 0.0441 | 0.3553 ± 0.0441 | 0.3366 ± 0.0441 | 0.0067 ± 0.0009 | 0.0071 ± 0.0009 | 0.0067 ± 0.0009 |
| 50 | 90% | 24 | 0.3824 ± 0.0588 | 0.3530 ± 0.0588 | 0.3530 ± 0.0588 | 0.0076 ± 0.1122 | 0.0071 ± 0.1122 | 0.0071 ± 0.1122 |
| | | 48 | 0.4301 ± 0.0441 | 0.4114 ± 0.0441 | 0.3927 ± 0.0441 | 0.0086 ± 0.0009 | 0.0082 ± 0.0009 | 0.0079 ± 0.0009 |
| 60 | 100% | 24 | 0.4118 ± 0.1122 | 0.3824 ± 0.1122 | 0.3824 ± 0.1122 | 0.0069 ± 0.0019 | 0.0064 ± 0.0019 | 0.0064 ± 0.0019 |
| | | 48 | 0.4488 ± 0.0935 | 0.4301 ± 0.0935 | 0.4114 ± 0.0935 | 0.0075 ± 0.0016 | 0.0072 ± 0.0016 | 0.0069 ± 0.0016 |
| 60 | 90% | 24 | 0.4707 ± 0.1122 | 0.4412 ± 0.1122 | 0.4118 ± 0.1122 | 0.0078 ± 0.0019 | 0.0074 ± 0.0019 | 0.0069 ± 0.0019 |
| | | 48 | 0.5236 ± 0.0935 | 0.4862 ± 0.0935 | 0.4488 ± 0.0935 | 0.0087 ± 0.0016 | 0.0081 ± 0.0016 | 0.0075 ± 0.0016 |

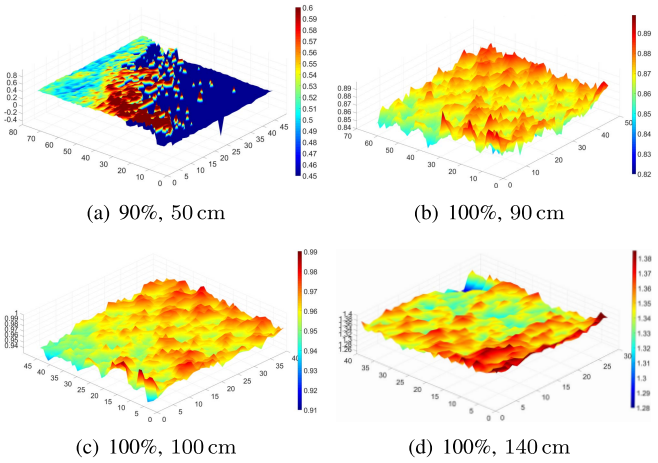

(a) 90%, 50 cm (b) 100%, 90 cm

(c) 100%, 100 cm (d) 100%, 140 cm

Fig. 13. Sine wave graphs were obtained by combining path 1 and path 2. (a) With 90% transmittance at 50 cm distance. (b) With 100% transmittance at 90 cm distance. (c) With 100% transmittance at 100 cm distance. (d) With 100% transmittance at 140 cm distance.

for the foam target, whether using single-frequency method or multi-frequency multipath recovery (Fig.12). The reason for this is that in the absence of dirt, MPI has already appeared in the measurements due to the concavities in the foam's surface. If dirt interference is added, the measurement results will be completely unreliable. Interestingly, in the case of multi-frequency multipath recovery with $K = 2$, the values measured through path $P_1$ (Fig.12(c)) and the values measured through path $P_2$ (Fig.12(d)) are complementary, i.e., points that were incorrectly measured from path $P_1$ were measured correctly from path $P_2$. This experiment was not designed to measure exact values but to observe the sine wave on the surface of the foam. The single-path cannot accurately reconstruct the sine wave image, so, a more accurate sine wave image can be realized by combining path $P_1$ and path $P_2$. In Fig.13(a), when the light transmittance is 90%, the sine wave shape on the foam surface cannot be observed. However, when the light transmittance is 100%, the pattern can be observed. As the distance between the camera and the foam becomes longer, the details of the pattern become blurred.

### D. Böhler Stars

A Böhler star is a device for measuring lateral resolution, which is a very important parameter for 3D cameras. The axial resolution $r_{\text{ax}}$ can be calculated as

$$r_{\text{ax}} = \frac{\pi d_p M}{n} \tag{9}$$

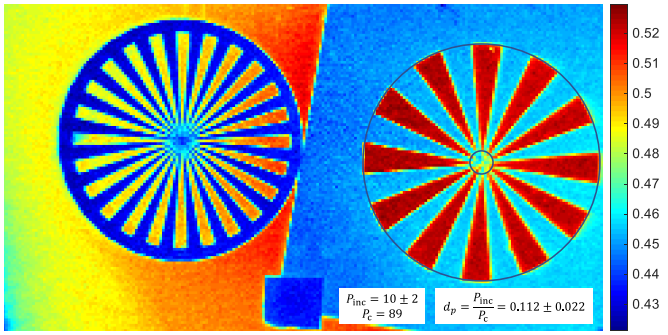


Fig. 14. Depth image of the two Böhler stars for the case of multi-frequency multipath recovery with $K = 1$ with 100% transmittance at 50 cm distance. $P_{\text{inc}}$ is the number of pixels occupied by the diameter of an incorrectly measured circle. $P_c$ is the number of pixels occupied by the diameter of the star.

We use two Böhler stars of 20cm diameter and number of fields $n = 48$ and $n = 24$, respectively (Fig.14). $d_p$ is the ratio between the diameter of the incorrectly measured circle in the middle of the star and the diameter $M$ of the star. From the axial resolution $r_{\text{ax}}$ and the distance $D$ between the camera and the Böhler star, we obtain the angular resolution $r_{\text{an}}$ as

$$r_{\text{an}} = \text{atan2}(r_{\text{ax}}, D) \tag{10}$$

In Fig.15, some of the resulting images are shown when the camera works in the *invalid* operation region (Fig.15(a)), when the camera works in the *reliable* operation region (Fig.15(b)) and Fig.15(c)), and when the camera works in the *unreliable* operation region (Fig.15(d)). In Fig.14 the $d_p$ is calculated by counting the image pixels.

Table.II shows the axial resolution and angular resolution in different cases. We can conclude from the Table.II that increasing the distance and decreasing the transmittance, whether in the case of the 24-fields Böhler star or the 48-fields Böhler star, will make the lateral resolution lower. In theory, the resolution measured via the 24-fields Böhler star and the 48-fields Böhler star should be identical under ideal conditions. However, when the camera works in the reliable operation region, the results obtained from our experiments show that the resolution measured by the 24-fields Böhler star is better than that measured by the 48-fields Böhler star. It is observed in both the 24- and the 48-fields Böhler star cases that the lateral resolution obtained with the multi-frequency multi-path approach is better than with the single-frequency approach. Consequently, we can conclude that using multiple frequencies

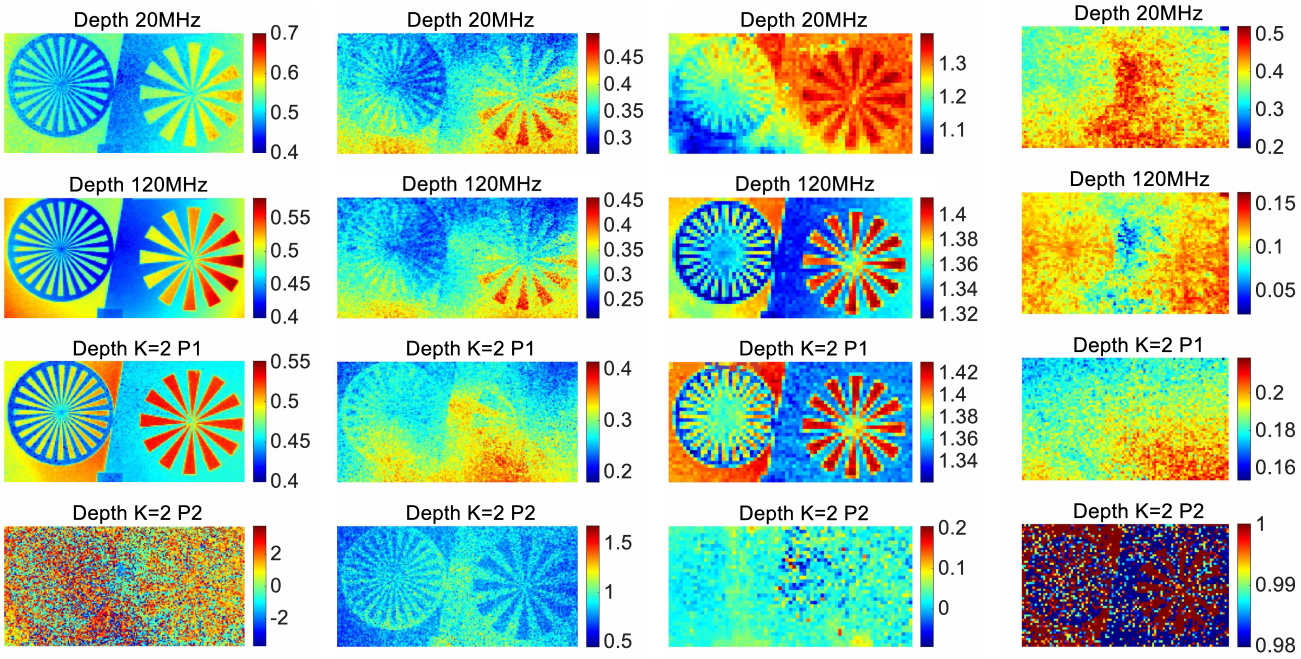


(a) 75%, 50 cm (b) 100%, 50 cm (c) 100%, 140 cm (d) 80%, 100 cm

Fig. 15. Depth plots of the two Böhler stars. (a) With 75% transmittance at 50 cm distance. (b) With 100% transmittance at 50 cm distance. (c) With 100% transmittance at 140 cm distance. (d) With 80% transmittance at 100 cm distance.

yields improved axial/angular resolution. A similar effect had been observed in [39], where an adaptive HDR (AHDR) sensing method was introduced to cope with the limited dynamic range of PMD ToF pixels. When implementing the AHDR method, the effective lateral resolution of the depth camera is increased by a factor three.

By comparing the depth images obtained by the camera in different operating areas using different methods for different targets, we demonstrate that the use of a multi-frequency approach can compensate to a certain extent for the degradation of the measurement accuracy of single-path measurements due to the influence of dust.

## V. Conclusion

Our work in this paper covers a relevant gap in the existing literature on the analysis of the effect of environmental factors on the performance of ToF cameras. We have conducted an extensive metrological evaluation of the effect of dust pollution on the performance of ToF cameras through several different experiments using customized sheets with different transmittances between 50% and 100%. In order to quantitatively analyze the effect of dust on the camera, customizing the sheets containing dust is also a crucial part of this experiment, for which we have also proposed a standard framework for obtaining the required samples of dust-polluted polycarbonate sheets of different transmittances.

Depending on the limited operating conditions of the 3D ToF camera in terms of varying light transmittance and distance, we have defined the camera operation into three stages: the *invalid* operation region, the *unreliable* operation region, and the *reliable* operation region. In a dirt-free environment, the 3D ToF camera has excellent performance, achieving 99.7% accuracy at a range of 1.5m. As the camera cover was gradually covered by dirt, the performance of the 3D ToF camera dropped dramatically.

Furthermore, we have adopted both classical single-frequency estimation (*four-phases algorithm*) of a single path and multi-frequency estimation (*matrix pencil method*) of several paths for each experimental target. Due to the presence of a secondary return path arising from the dirty sensor cover, the single-path assumption no longer holds. The multi-frequency approach was found to perform better than single-frequency methods for retrieving the true depth under the effect of dust, since it allows for distinguishing more than a single return path.

Among the subjects of future work, studying the detailed performance of the camera working in the reliable work area (light transmittance between 90% and 100%) has become a meaningful subject for future studies, at the light of the results obtained in this work. Another attractive line or work is the development of compensation methods, in combination with multi-frequency recovery under laboratory conditions, thus further increasing the depth estimation accuracy in the reliable regions, or even expanding the latter.

## References

[1] S. Huang, F. Gu, Z. Cheng, and Z. Song, "A joint calibration method for the 3D sensing system composed with ToF and stereo camera," in *Proc. IEEE Int. Conf. Inf. Autom. (ICIA)*, Aug. 2018, pp. 905–910.

[2] Y. He and S. Chen, "Recent advances in 3D data acquisition and processing by time-of-flight camera," *IEEE Access*, vol. 7, pp. 12495–12510, 2019.

[3] M. Van den Bergh and L. Van Gool, "Combining RGB and ToF cameras for real-time 3D hand gesture interaction," in *Proc. IEEE Workshop Appl. Comput. Vis. (WACV)*, Jan. 2011, pp. 66–72.

[4] G. Simion and C.-D. Caleanu, "A ToF 3D database for hand gesture recognition," in *Proc. 10th Int. Symp. Electron. Telecommun.*, Nov. 2012, pp. 363–366.
[5] C. Distante, G. Diraco, and A. Leone, "Active range imaging dataset for indoor surveillance," in *Proc. Brit. Mach. Vis. Conf. (BMVC)*, vol. 2, 2010, pp. 1–16. [Online]. Available: http://www.bmva.org/annals/2010/2010-0003.pdf
[6] M. H. Conde, "A material-sensing time-of-flight camera," *IEEE Sensors Lett.*, vol. 4, no. 7, pp. 1–4, Jul. 2020.
[7] M. H. Conde, T. Kerstein, B. Buxbaum, and O. Loffeld, "Near-infrared, depth, material: Towards a trimodal time-of-flight camera," in *Proc. IEEE Sensors*, Oct. 2020, pp. 1–4.
[8] J. Steinbaeck, A. Tengg, G. Holweg, and N. Druml, "A 3D time-of-flight mixed-criticality system for environment perception," in *Proc. Euromicro Conf. Digit. Syst. Design (DSD)*, Aug. 2017, pp. 368–374.
[9] S. Foix, G. Alenya, and C. Torras, "Lock-in time-of-flight (ToF) cameras: A survey," *IEEE Sensors J.*, vol. 11, no. 9, pp. 1917–1926, Sep. 2011, doi: 10.1109/JSEN.2010.2101060.
[10] A. Bhandari *et al.*, "Resolving multipath interference in time-of-flight imaging via modulation frequency diversity and sparse regularization," *Opt. Lett.*, vol. 39, no. 6, pp. 1705–1708, Mar. 2014.
[11] A. Bhandari, A. Kadambi, and R. Raskar, "Sparse linear operator identification without sparse regularization? Applications to mixed pixel problem in time-of-flight/range imaging," in *Proc. IEEE Int. Conf. Acoust., Speech Signal Process. (ICASSP)*, May 2014, pp. 365–369.
[12] A. Bhandari, M. H. Conde, and O. Loffeld, "One-bit time-resolved imaging," *IEEE Trans. Pattern Anal. Mach. Intell.*, vol. 42, no. 7, pp. 1630–1641, Jul. 2020.
[13] A. Bhandari and R. Raskar, "Signal processing for time-of-flight imaging sensors: An introduction to inverse problems in computational 3-D imaging," *IEEE Signal Process. Mag.*, vol. 33, no. 5, pp. 45–58, Sep. 2016.
[14] A. Kirmani, A. Benedetti, and P. A. Chou, "SPUMIC: Simultaneous phase unwrapping and multipath interference cancellation in time-of-flight cameras using spectral methods," in *Proc. IEEE Int. Conf. Multimedia Expo. (ICME)*, Jul. 2013, pp. 1–6.
[15] D. Piatti, "Time-of-flight cameras: Tests, calibration and multi-frame registration for automatic 3D object reconstruction," Ph.D. dissertation, Polytechnic Univ. Turin, Turin, Italy, 2011.
[16] A. P. P. Jongenelen, D. G. Bailey, A. D. Payne, A. A. Dorrington, and D. A. Carnegie, "Analysis of errors in ToF range imaging with dual-frequency modulation," *IEEE Trans. Instrum. Meas.*, vol. 60, no. 5, pp. 1861–1868, May 2011.
[17] M. Lindner and A. Kolb, "Lateral and depth calibration of PMD-distance sensors," in *Proc. Int. Symp. Vis. Comput.*, Nov. 2006, pp. 524–533.
[18] H. Shim *et al.*, "Time-of-flight sensor and color camera calibration for multi-view acquisition," *Vis. Comput.*, vol. 28, no. 12, pp. 1139–1151, Dec. 2012.
[19] J. P. Godbaz, M. J. Cree, and A. A. Dorrington, "Closed-form inverses for the mixed pixel/multipath interference problem in AMCW lidar," *Proc. SPIE*, vol. 8296, pp. 829618-1–829618-15, Feb. 2012.
[20] J. Lin, Y. Liu, M. B. Hullin, and Q. Dai, "Fourier analysis on transient imaging with a multifrequency time-of-flight camera," in *Proc. IEEE Conf. Comput. Vis. Pattern Recognit.*, Jun. 2014, pp. 3230–3237.
[21] Y. Hua and T. K. Sarkar, "Matrix pencil method for estimating parameters of exponentially damped/undamped sinusoids in noise," *IEEE Trans. Acoust., Speech, Signal Process.*, vol. 38, no. 5, pp. 814–824, May 1990.
[22] A. Bhandari, M. Feigin, S. Izadi, C. Rhemann, M. Schmidt, and R. Raskar, "Resolving multipath interference in Kinect: An inverse problem approach," in *Proc. IEEE Sensors*, Nov. 2014, pp. 614–617.
[23] A. Bhandari, A. M. Wallace, and R. Raskar, "Super-resolved time-of-flight sensing via FRI sampling theory," in *Proc. IEEE Int. Conf. Acoust., Speech Signal Process. (ICASSP)*, Mar. 2016, pp. 4009–4013.
[24] V. N. Xuan, K. Hartmann, W. Weihs, and O. Loffeld, "Multi-target super-resolution using compressive sensing arguments for multipath interference recovery," in *Proc. 4th Int. Workshop Compressed Sens. Theory Appl. Radar, Sonar Remote Sens. (CoSeRa)*, Sep. 2016, pp. 148–152.
[25] M. Heredia Conde, K. Hartmann, and O. Loffeld, "A compressed sensing framework for accurate and robust waveform reconstruction and phase retrieval using the photonic mixer device," *IEEE Photon. J.*, vol. 7, no. 3, pp. 1–16, Jun. 2015.
[26] M. Heredia Conde, "Compressive sensing for the photonic mixer device," in *Compressive Sensing for the Photonic Mixer Device*. Wiesbaden, German, Springer, 2017, pp. 207–352.
[27] M. Heredia Conde, T. Kerstein, B. Buxbaum, and O. Loffeld, "Fast multipath estimation for PMD sensors," in *Proc. 5th Int. Workshop CS. Theory App. Radar Sonar Remote Sens. (CoSeaRa)*, Siegen, Germany, Sep. 2018, pp. 1–6.
[28] J. Marco *et al.*, "DeepToF: Off-the-shelf real-time correction of multipath interference in time-of-flight imaging," *ACM Trans. Graph. (ToG)*, vol. 36, no. 6, pp. 1–12, 2017.
[29] R. H. Rasshofer, M. Spies, and H. Spies, "Influences of weather phenomena on automotive laser radar systems," *Adv. Radio Sci.*, vol. 9, pp. 49–60, Jul. 2011.
[30] J. R. V. Rivero *et al.*, "Characterization and simulation of the effect of road dirt on the performance of a laser scanner," in *Proc. IEEE 20th Int. Conf. Intell. Transp. Syst. (ITSC)*, Oct. 2017, pp. 1–6.
[31] M. Baumgart, C. Consani, M. Dielacher, and N. Druml, "Optical simulation of time-of-flight sensor accuracy in rain," in *Proc. Conf. Lasers Electro-Optics Eur. Eur. Quantum Electron. Conf. (CLEO/Eur.-EQEC)*, Jun. 2017.
[32] M. Trierweiler, P. Caldelas, G. Groninger, T. Peterseim, and C. Neumann, "Influence of sensor blockage on automotive LiDAR systems," in *Proc. IEEE Sensors*, Oct. 2019, pp. 1–4.
[33] Y. Li, P. Duthon, M. Colomb, and J. Ibanez-Guzman, "What happens for a ToF LiDAR in fog?" *IEEE Trans. Intell. Transp. Syst.*, vol. 22, no. 11, pp. 6670–6681, Nov. 2021.
[34] *Table 4: Air Cleaner Test Code*, Standard SAE J726, SAE International, Air Cleaner Test Code Standards Committee, Jun., 1993.
[35] M. H. Conde, A. Bhandari, T. Kerstein, B. Buxbaum, and O. Loffeld, "Live demonstration: Multiple-path depth imaging with time-of-flight sensors," in *Proc. IEEE Sensors*, Oct. 2019, p. 1.
[36] T. Möller, H. Kraft, J. Frey, M. Albrecht, and R. Lange, "Robust 3D measurement with PMD sensors," in *Proc. 1st Range Imag. Res. Day (ETH)*, Sep. 2005, p. 906.
[37] T. Ringbeck, T. Möller, and B. Hagebeuker, "Multidimensional measurement by using 3-D PMD sensors," *Adv. Radio Sci.*, vol. 5, pp. 135–146, Jun. 2007. [Online]. Available: https://ars.copernicus.org/articles/5/135/2007/ars-5-135-2007.pdf
[38] M. H. Conde, "Raw data processing for practical time-of-flight super-resolution," in *Proc. IEEE Int. Conf. Acoust., Speech Signal Process. (ICASSP)*, Jun. 2021, pp. 1650–1654.
[39] M. H. Conde, K. Hartmann, and O. Loffeld, "Adaptive high dynamic range for time-of-flight cameras," *IEEE Trans. Instrum. Meas.*, vol. 64, no. 7, pp. 1885–1906, Jul. 2015.

**Zhibin Liu** received the B.S. degree from the University of Zhengzhou, Zhengzhou, China, in 2016 and the M.S. degree in automation and energy technology from the University of Siegen, Siegen, Germany, in 2022. He is a Research Assistant with the Center for Sensor Systems (ZESS). University of Siegen. His current research interests include visible light communication, time-of-flight imaging systems, and their applications to the field of indoor positioning.

**Miguel Heredia Conde** (Member, IEEE) received the Dr. Eng. degree in sensor signal processing from the University of Siegen, Siegen, Germany, in 2016.

In 2013, he joined the Center for Sensor Systems (ZESS), University of Siegen. Since 2013, he has been a member of the Research Training Group GRK 1564 "Imaging New Modalities." Since 2016, he has been the Leader of the "Compressive Sensing for the Photonic Mixer Device" Research Group and the General Manager of the H2020-MSCA-ITN "MENELAOS$^{NT}$," since 2020. His current research interests include time-of-flight imaging systems, such as those based on the photonic mixer device (PMD), compressive sensing, computational imaging, and unconventional sensing.

Dr. Miguel Heredia was a recipient of the 2006 Academic Excellence Prices, awarded by the Government of Galicia, Spain, and the University of Siegen Prize for International Young Academics, for the excellent performance in his doctoral studies, in 2017. He is a member of ITG/VDE and SPS.